Generation of series of electron acoustic solitary wave pulses in plasma

View Online   Export Citation   CrossMark

Amar Kakad[a] (iD) and Bharati Kakad[b] (iD)

AFFILIATIONS

Indian Institute of Geomagnetism, New Panvel, Navi Mumbai 410-218, India

[a]amar@iigs.iigm.res.in
[b]ebharati@iigs.iigm.res.in

ABSTRACT

One-dimensional fluid simulation is used to investigate the generation of electron-acoustic solitary waves (EASWs) in three-species plasma. We consider an unmagnetized collisionless plasma consisting of cold electrons, hot electrons, and ions. The Gaussian perturbations in the equilibrium electron and ion densities are used to excite the waves in the plasma. This simulation demonstrates the generation of a series of EASW pulses in this three-species plasma through the process of wave breaking. We investigate the behavior of the ponderomotive potential, frequency, and force associated with electrons and ions during the process of the wave breaking. We observed that the ponderomotive potential of the hot electron, which is the driving species for the electron acoustic waves, peaks at the time of wave breaking. The variation of the maximum ponderomotive force acting spatially on the leading and trailing edges of the hump in the cold and hot electron and ion fluid densities shows the maximum imbalance in the magnitude of the ponderomotive force acting on both sides of the hot electron density hump at the time of wave breaking. This reveals that the imbalanced ponderomotive force acting on the hot electron fluid is responsible for the breaking of the electron acoustic wave in plasma. Furthermore, it is observed that the wave breaking process occurs at an earlier time if the hot electron temperature is increased.

I. INTRODUCTION

An electron acoustic (EA) wave is a high-frequency wave (in comparison with the ion plasma frequency) that occurs in plasma with two distinct populations of electrons with different temperatures, referred to as cold and hot electrons.[1,2] It is an electrostatic wave in a plasma, in which the restoring force comes from the pressure of the hot electrons, while the inertia comes from the cold electron population. The ions play the role of a neutralizing background as their dynamics does not influence the EA waves because the EA wave frequency is much higher than the ion plasma frequency. It is known that the phase speed of the EA waves must be intermediate between the cold and hot electron thermal speeds such that the wave damping by both the cold and hot electron species is negligible. The EA wave can also exist in two-component plasma consisting of electrons and ions with ion thermal velocity greater than electron thermal velocity.[3]

It is well known that the two electron temperature plasmas occur both near the Earth space plasma environment[4–9] and in laboratory plasma.[10–12] In the Earth's magnetosphere, the most prominent regions are the boundary layer regions, where the cold electrons from one region mix up with the hot electron population of the adjacent region. Thus, these boundary layer regions of the Earth's magnetosphere are most favorable regions for the existence of EA waves. Over the past few decades, many satellites (e.g., Polar, GEOTAIL, FAST, Cluster, and Van Allen Probes) have observed the EA waves in various regions of the Earth's magnetosphere, e.g., Earth's magnetosheath region,[13] the plasma sheet boundary layer region,[14] the magnetotail region,[15,16] the day-side auroral acceleration region,[4,5] the radiation belt region,[7,9,17] etc.

The nonlinear propagation of electron-acoustic solitary waves (EASWs) in an unmagnetized two-electron plasma has been considered by several authors.[9,13,14,16,18–23] These studies are based on Sagdeev's pseudopotential formalism, which yields nonlinear stationary solutions for arbitrary amplitude solitons. In this formalism, the fluid equations of the plasma species are combined with Poisson's equation to yield the energy integral of a particle with unit mass in a potential well. The pseudopotential determines whether the existence of soliton shaped wave structures in the potential having bipolar electric field signatures is possible or not. However, the pseudopotential technique has a limitation due to its inability to provide the time evolution of multiple wave structures at a time. Recently,

Kakad et al.[24] and Kakad and Kakad[25] performed one-dimensional fluid simulations to address the evolutionary characteristics of ion acoustic waves in plasma. They compared their simulation results with the nonlinear fluid theory and confirmed their stable propagation. Apart from this, they have also noticed the formation of chains of ion acoustic solitary wave structures through the process of wave breaking in two-component (electron and ion) plasma. However, we do not know whether such a process is observed for electron acoustic wave mode or not. The validity of ponderomotive potential as a proxy of the breaking of an ion acoustic wave is tested under fluid[26] and kinetic regimes.[27] However, whether these proxies are applicable to other wave modes or not is not yet known. Motivated by these studies, we perform the fluid simulation of EASWs in plasma. This paper is structured as follows: the simulation model is briefly discussed in Sec. II. The simulation results are presented in Sec. III. We summarize our conclusions in Sec. IV.

II. PLASMA MODEL

We consider a homogeneous, collisionless three-component plasma consisting of fluid cold and hot electrons and fluid ions (H^+). In this study, we retain the pressure and inertia of all the species considered in the model.[20,21,28,29] For the nonlinear EA waves propagating parallel to the magnetic field, the dynamics of the system is governed by the fluid equations, viz., the continuity, momentum, and pressure equations of each species, and the Poisson equation[20,21,29] given by

$$\frac{\partial n_j}{\partial t} + \frac{\partial (n_j v_j)}{\partial x} = 0, \tag{1}$$

$$\frac{\partial v_j}{\partial t} + v_j \frac{\partial v_j}{\partial x} + \frac{1}{m_j n_j}\frac{\partial P_j}{\partial x} - \frac{Z_j}{m_j}E = 0, \tag{2}$$

$$\frac{\partial P_j}{\partial t} + v_j \frac{\partial P_j}{\partial x} + \gamma_j P_j \frac{\partial v_j}{\partial x} = 0, \tag{3}$$

$$\epsilon_0 \frac{\partial E}{\partial x} = \sum_j Z_j n_j. \tag{4}$$

The electric field (E) can be written in terms of an electrostatic potential (ϕ) as $E = -\partial\phi/\partial x$. In the equations listed above, the subscripts $j = ce$, he, and i are used for cold electrons, hot electrons, and ions, respectively. The variables n_j, P_j, and v_j are the plasma density, thermal pressure, and velocity of the species j, respectively. Here, m_j and Z_j represent the mass and charge of the species j, respectively. The charge is $Z_e = -e$ for electrons and $Z_i = e$ for ions. ϵ_0 is the electric permittivity. In Eq. (3), i.e., the equation of state, we have treated electrons to be isothermal with $\gamma_{ce} = \gamma_{he} = 1$ and ions to be adiabatic with $\gamma_i = 3$.

In the development of the fluid code, the above set of equations is solved by using numerical schemes that are discussed in Kakad et al.[24] In the simulation code, the spatial derivatives of the physical quantities in Eqs. (1)–(4) are computed using the finite difference scheme,[24,29–33] which is accurate to the fourth-order. We integrate Eqs. (1)–(3) in time by the leap-frog method,[24,29–33] which is accurate to the second order. The leap-frog method gives rise to a grid separation numerical instability. We have used a compensated filter to eliminate the small wavelength modes linked with such numerical instability.[24,29–33] A necessary condition for the convergence of the explicit finite difference method used in our simulation is that it has constrained by the Courant-Friedrichs-Lewy (CFL) condition, $V_{max}\frac{\Delta t}{\Delta x} \leq 1$. Δx and Δt represent the grid size in spatial and time domains, respectively. In the

present simulation, these parameters are chosen in such a way that the Courant condition is always fulfilled.

III. SIMULATION RESULTS

We perform the fluid simulations in a one-dimensional system with the periodic boundary conditions. For all simulation runs, we assume an artificial ion to electron mass ratio $m_i/m_e = 100$. The flow velocities of the electrons and the ions are assumed to be zero initially, i.e., at $t = 0$, $v_{dce}(x) = v_{dhe}(x) = v_{di}(x) = 0$. The background electron and ion densities are set in such a way that the system satisfies the quasineutrality, i.e., $n_{ce0} + n_{he0} = n_{i0} = n_0 = 1$. The values of ω_{pi}, ω_{pce}, and ω_{phe} are 0.1, 0.95, and 0.32, respectively. We used the localized Gaussian type initial density perturbation (IDP) in the equilibrium electron and ion densities given by

$$\delta n = \Delta n \ \exp\left[-\left(\frac{x - x_c}{l_0}\right)^2\right]. \tag{5}$$

In Eq. (5), Δn and l_0 are the amplitude and width of the superimposed IDP, respectively. Here, x_c is the center of the simulation system. Thus, the perturbed densities $n_j(x) = n_{j0} + \delta n$ take the following form as the initial condition:

$$n_j(x) = n_{j0} + \Delta n \ \exp\left[-\left(\frac{x - x_c}{l_0}\right)^2\right]. \tag{6}$$

We perform the fluid simulations for a different hot electron to cold electron temperature ratio (T_{he}/T_{ce}) to investigate its effect on the evolution of a series of EASW structures in plasma. In the simulation, we varied the electron temperature ratio as $T_{he}/T_{ce} = 300$, 500, and 700. Furthermore, the ion to cold electron temperature ratio is the same for all simulation runs at $T_i/T_{ce} = 100$. Here, T_{ce} is taken as 0.01. For all simulation runs, we took time interval $dt = 8 \times 10^{-3}$, the grid spacing $dx = 0.2$, "system length" $L_x = 7000$, $l_0 = 30$, and $\Delta n = 0.5$. Here, l_0 and Δn are chosen in such a way that the breaking of EA waves occurs for the plasma parameters considered in the simulation. Different parameters used in the simulations are given in Table I. The plasma parameters used in the simulation are taken from Lakhina et al.[20]

A. Evolution of stable EASWs

We first undertake a discussion of the generation and evolution of a series of EASW structures when the IDPs are used to perturb the background electron and ion densities in the fluid simulation. In a plasma consisting of cold electrons, hot electrons, and ions with no applied magnetic field, the IDP creates charge separations that drive the EASWs in the system. Here, we discuss the evolution of the series of EASW structures for simulation run (run-1). Some of the physical

TABLE I. Parameters used in the simulation runs to investigate the effect of hot electron temperature on the onset time of the steepening and breaking of the EA wave.

Run	T_{he}	v_{the}	m_e	m_i	n_{ce}	n_{he}	n_i	v_{dce}	v_{dhe}	v_{di}	v_{tce}	v_{ti}	T_{ce}	T_i
1	3	1.73	1	100	0.9	0.1	1	0	0	0	0.1	0.1	0.01	1
2	5	2.24												
3	7	2.65												

quantities evolved at different stages are shown in Fig. 1. The panels in the first and second rows of this figure show deviation in densities with respect to their ambient densities (i.e., $n_j - n_{j0}$) and velocities for hots electron, cold electrons, and ions at different times, $t = 0, 46, 80$, and 152, respectively. Here, hot electron velocity is divided by 10 to visualize the variations of all species on the same scale in the figure. The panels in the third and fourth rows show the evolution of the electric field and electrostatic potential at respective times, respectively. The panels at $t = 0$ show the initial setup of the simulation when the IDP is introduced in the uniform plasma density. At this stage, the injection of the IDP causes charge separation in the plasma that sets up an infinitesimal electrostatic potential, which grows with time and evolves into two oppositely propagating EA pulses along with the EA oscillations located close to the center of the simulation system. One of the snapshots of the evolved electrostatic potential (fourth row of Fig. 1) associated with such EA pulses is shown at $t = 46$. Both EA pulses are found to be weakly nonlinear and have longer wavelengths. These EA pulses are indistinguishable and propagate toward the opposite boundaries of the simulation system. Later, during their propagation, the amplitude and speed of the EA pulses gradually increase until

the critical speed is reached. Consequently, the leading edge of both pulses tends to steepen at time $t = 80$. One of the snapshots of such pulses is shown in Fig. 1(c). Because of the steepening process, the amplitude of the EA pulses increases, and then these EA pulses collapse through the wave breaking process at $t = 152$ as depicted in Fig. 1(d). Once initiated, the wave breaking process continues until the formation of two chains of unstable short wavelength EASW pulses. These unstable EASW pulses in these chains eventually evolved into the stable EA solitons after a long time. The formation of one of the chains of EASW pulses can be seen in supplementary material (file A1), where the evolution of the electric field and electrostatic potential associated with the EASW pulses is shown.

It may be noted that we observe the hump in hot electron density and dip in cold electron density, which are associated with EASWs [see upper panels of Figs. 1(b)–1(d)]. The theoretical study by Watanabe and Taniuti[1] suggested that in three-species plasma, the inertia provided by the cold electrons and the restoring force coming from the pressure of the hot electrons help in maintaining the EASW structures. Also, these authors have mentioned that the deviation in hot electron and cold electron densities at the location of the EA pulse
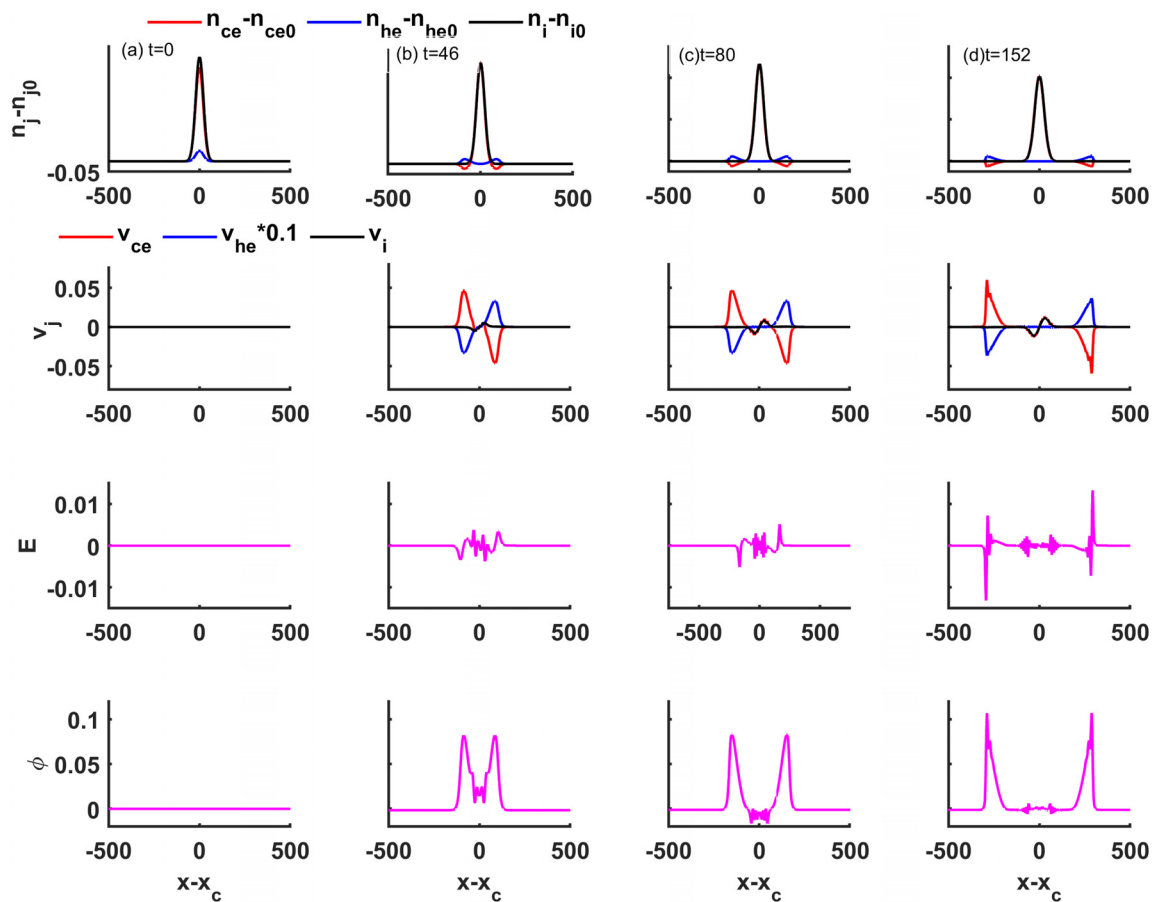
FIG. 1. Snapshots of the evolution of EASWs from the simulation run-1. The deviation in densities with respect to their ambient values, velocities, electric field, and electrostatic potential is shown at (a) $t = 0$ (initial time), (b) $t = 46$ (at the time when two indistinguishable EA pulses are formed), (c) $t = 80$ (time when steepening initiated), and (d) $t = 152$ (time when the wave breaking initiated).

holds $\delta n_{he} = -\delta n_{ce}$. In our simulation, we have verified this and confirm that EASWs follow this condition. The upper panel in Figs. 1(b)–1(d) clearly shows the dip in cold electron density and hump in hot electron density, which are of the same magnitude. On the other hand, the ion density shows a single nonpropagating hump at the center of the system, which shows that the ions do not play any role in the dynamics of EASWs. This is expected as ion plasma frequency is much smaller compared to electron plasma frequency and hence ion dynamics does not influence the propagation of EASWs in plasma.

B. Spatiotemporal evolution and dispersion characteristics of EASWs

We examined the evolution and propagation of different wave structures through the spatial and temporal evolution of their electrostatic potential and associated electric field in the simulation, which are depicted in Figs. 2(a) and 2(b), respectively. In this figure, $x - x_c = 0$ represents the center of the simulation system. As the modes propagating away from the center toward the left and right boundaries of the system are indistinguishable, we have shown only the wave mode propagating in the right-side. One can see that the initially excited EA wave pulse breaks into the chain of EASW structures during its evolution. The chain contains five distinguishable pulses with different peak amplitudes and widths, which can be identified with the different colors in Fig. 2. It is observed that the large amplitude pulse propagates faster as compared to the subsequent small amplitude pulse in the chain. These pulses in the chain get separated from each other due to the difference in their phase speeds. After a sufficiently long time, each of the pulses in the chain propagates stably by retaining their shape and size in the system, which is one of the characteristics of the soliton type structures in plasma. The speed of each solitary

wave in the chain can be obtained from the slope of the respective color band of the wave pulse in this spatiotemporal plot. For these EASW pulses, the estimated phase speeds are found to be 1.79, 1.76, 1.73, 1.70, and 1.69, respectively, during their stable propagation. The linear dispersion relation for EA waves in three-species plasma is given by the following equation:

$$1 - \sum_s \frac{\omega_{ps}^2}{\omega^2 - \gamma_s k^2 v_{ts}^2} = 0. \tag{7}$$

In this case, the phase speed of EASW mode based on its linear dispersion relation comes out to be $V_s = 1.65$ in the short wavelength regime (k > 0.8). To confirm the existence of different modes in the simulation system, we obtained the ω–k diagram by taking the Fourier transform of the electrostatic potential in space and time. For run-1, the ω–k plot for the period $t = 0$–240 is shown in Fig. 3. The resolution of this dispersion plot is 0.026 in the frequency domain. The speed obtained from the linear dispersion is plotted with the dashed white lines over the dispersion plot obtained from the simulation in Fig. 3. This confirms that the two outer dispersion curves in this figure that extend above the cold electron plasma frequency (ω_{pce}) are electron acoustic modes, whereas the other dispersion curves starting at $\omega \geq \omega_{pce}$ correspond to the Langmuir modes.

To compare the evolution of the EASWs with the other simulation runs, we depicted the spatial and temporal evolution of the electrostatic potential and the electric field of simulation run-3 in Fig. 4. In this case, it is seen that the IDP evolves into two chains of EASW pulses, wherein each chain contains four EASW pulses. During their stable propagation, the phase speeds of these four pulses are estimated to be 2.7, 2.65, 2.6, and 2.55, respectively. The animation of the formation and evolution of the chain of EASWs in this simulation run is
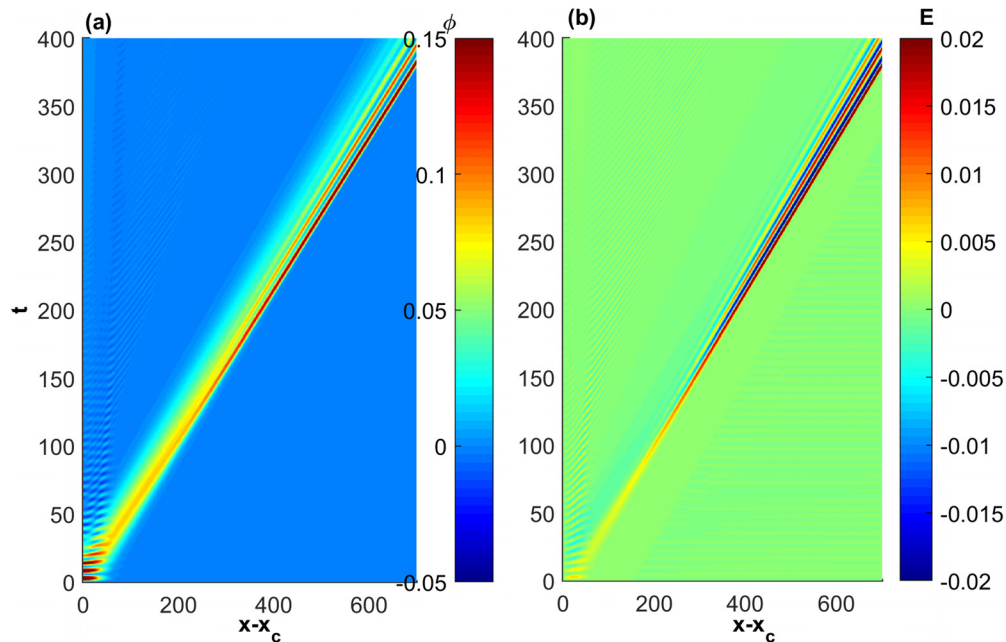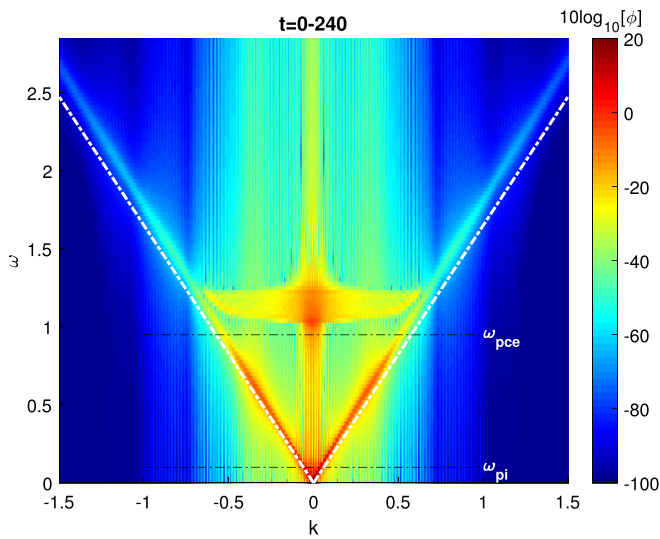

FIG. 2. Spatial and temporal evolution of electrostatic potential (panel-a) and electric field (panel-b) for the simulation run-1. The different color bands in these panels correspond to the chain of electron acoustic pulses propagating toward the right-side boundary of the system.
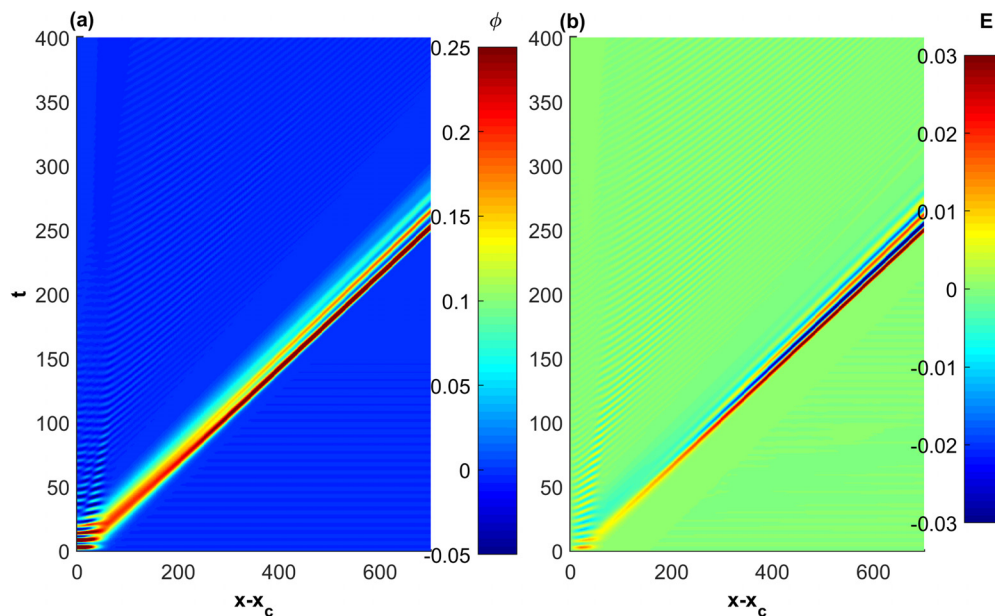
FIG. 3. Ω–k dispersion diagram obtained from the electrostatic potential during $t = 0$–240 of run-1. It shows the presence of both Langmuir and electron acoustic modes. The speed of electron acoustic mode ($V_s = 1.65$) estimated from its standard linear dispersion equations is shown with the slanted dashed-dotted lines. The cold electron (ion) plasma frequency is shown with a horizontal black line at $\omega_{pce} = 0.95$ ($\omega_{pi} = 0.1$).

shown in supplementary material (file A2). To examine the dispersion characteristics of the evolved modes, we have analyzed the two-dimensional Fourier transform of the spatiotemporal variation of the electrostatic potential obtained during $t = 0$–240, which is shown in Fig. 5. This figure shows two sets of dispersion curves. For the

considered simulation parameters, the linear dispersion relation gives the phase speed of $V_s = 2.5$ in the short wavelength regime (k > 0.6), which is shown with the white dashed lines in Fig. 5. This figure demonstrates that the outer dispersion curves are associated with the evolved EASW pulses in the simulation. The upper dispersion curves originating at the frequency above ω_{pce} are associated with Langmuir waves evolved in the system.

C. Ponderomotive force at the breaking of EASWs

In recent studies, the breaking process of ion acoustic waves and the formation of a chain of solitary structures in thermal[25] and non-thermal[26] plasmas have been examined in detail. These studies have pointed out the role of ponderomotive force (F_p) in the steepening and breaking of the ion acoustic waves. However, we do not know whether the ponderomotive potential as a proxy for the wave breaking process is applicable to EA wave mode or not. In this section, we have examined the time variation of ponderomotive force and potential during the evolution of EASWs. The ponderomotive force is an average second-order force that acts on a plasma resulting from spatially nonuniform oscillating fields. This force yields a modification of the average plasma profile, thereby causing a quasilinear modification of the stability characteristics of the original high-frequency oscillating fields. The charged particles execute a simple harmonic motion in response to an oscillating wave-field in plasma. In the case of a uniform field, these particles return to their initial position after one cycle of oscillation. In the case of a nonuniform field, the force exerted on the charge particles during the half-cycle spent in the area of higher amplitude field points in the direction where the field is weaker. It is larger than the force exerted during the half-cycle spent in the area with a lower amplitude field, which points toward the strong field area. Thus, averaged over a full cycle, there is a net force that drives the charge

FIG. 4. Spatial and temporal evolution of electrostatic potential (panel-a) and electric field (panel-b) for simulation run-3. The different color bands in these panels correspond to the chain of electron acoustic pulses propagating in a right-side boundary of the simulation system.
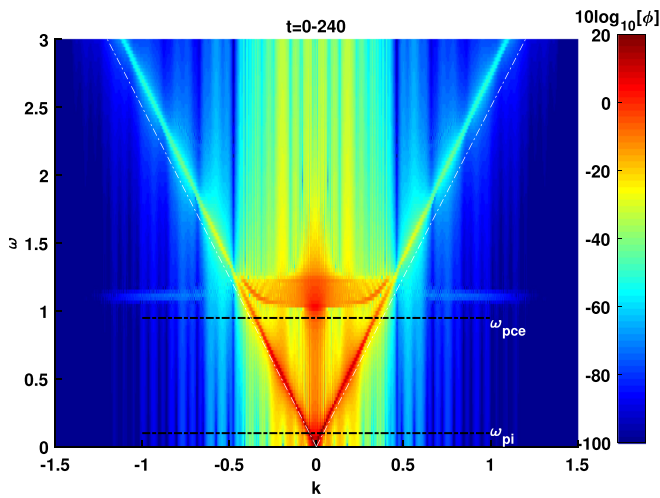
FIG. 5. Ω–k dispersion diagram obtained from the electrostatic potential during $t = 0$–240 of run-3. It shows the presence of both Langmuir and electron acoustic modes. The speed of electron acoustic mode ($V_s = 2.5$) estimated from its standard linear dispersion equations is shown with slanted white dashed lines. The cold electron (ion) plasma frequency is shown with a horizontal black line at $\omega_{pce} = 0.95$ ($\omega_{pi} = 0.1$).

FIG. 6. The schematic representation of the direction of ponderomotive force acting on the sides of the electrostatic Gaussian potential pulse. The red and blue arrows show the force acting on the right ($+x$) and left ($-x$) directions at points C and A, respectively. The bottom panel shows the behavior of ponderomotive force, which is proportional to $-\nabla|E|^2$ for this Gaussian potential pulse.

particles toward the weak field area. In one-dimension, the ponderomotive force experienced by the charged particles due to the nonuniform electric field oscillating at frequency Ω, i.e., $E(x, t) = E_0(x) \cos(\Omega t)$ is

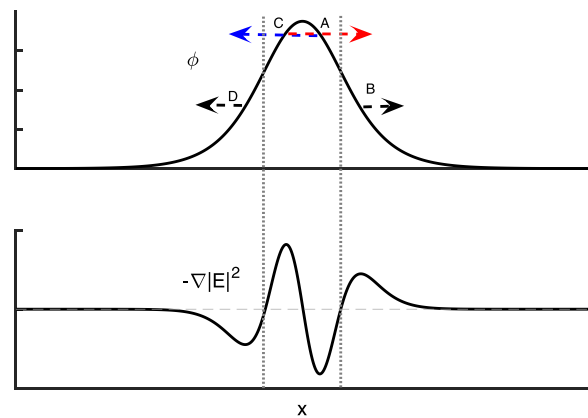$$F_p = \frac{-q_s^2}{4m_s\Omega^2}\frac{\partial}{\partial x}|E|^2 = -q_s\nabla\psi_p. \tag{8}$$

In the equation above, ψ_p is the ponderomotive potential defined as

$$\psi_p = \frac{q_s}{4m_s\Omega^2}|E|^2. \tag{9}$$

By rearranging the terms in Eq. (8), one can write the expression for ponderomotive frequency as

$$\Omega^2 = \frac{U}{KE_s}\frac{\omega_{ps}}{4}, \tag{10}$$

where q_s and m_s are the electrical charge and mass of the species s, respectively. Ω is the angular frequency of oscillation of the electric field E. Here, the electrostatic energy and kinetic energy of species s are represented by U and KE_s, respectively. This equation means that a charged particle in an inhomogeneous oscillating field not only oscillates at the frequency of Ω of the field but also is accelerated by F_p toward the region of a weak field. This is a case where the sign of the charge on the particle does not change the direction of the force. Also, this force is stronger for electrons as compared to ions. The schematic in Fig. 6 shows the directions of the ponderomotive force acting on the left- and right-sides of the positive amplitude electrostatic soliton-type potential structure. The variation of electrostatic potential (top panel) and $-\nabla|E|^2$ (bottom panel) is shown in this figure. In regions C and B, the ponderomotive force is in the $+x$ direction, whereas in regions A and D, the ponderomotive force is in the $-x$ direction. The vertical black dotted lines in Fig. 6 represent the position where

ponderomotive force is zero. Thus, the ponderomotive force pushes the plasma in regions A and C toward the center of the pulse. On the other hand, in regions B and D, the plasma is pushed away from the center of the pulse. The ponderomotive force is proportional to $-\nabla|E|^2$; thus, the magnitude of the force in regions A and C is larger as compared to that in regions B and D.

We investigated the steepening and breaking of the EA waves in detail for run-1. Figure 7 shows the variation of the maximum velocities (V_{jmax}), maximum ponderomotive potentials (Ψ_{jmax}), and average ponderomotive frequencies ($\langle\Omega_j\rangle$) of all species in the system. The dotted vertical lines labeled with t_1, t_2, and t_3 represent the time at which the two initial EA pulses are formed, the time at which the wave steepening process initiated, and the time at which the breaking of the EA wave pulse started, respectively. Now, the question is how do we get t_1, t_2, and t_3 from the simulations. The time of formation of two EA pulses at the initial stage is obtained by observing the evolution of the electric field and potential after introducing the IDP in the simulation system. The time of maximum phase speed attained by the initially formed unstable EASWs is referred to as the time of initiation of steepening [see Fig. 10(b)]. The time of the peak in the variation of maximum ponderomotive potential is taken as the time of initiation of wave breaking. These proxies to identify the time of steepening and wave breaking were proposed by Kakad and Kakad[25] for ion acoustic solitary waves (IASWs). It may be noted that in the present simulation, we have three species, namely, hot electrons, cold electrons, and ions. As seen in Fig. 7(b), the maximum ponderomotive potential associated with these species shows a clear peak near wave breaking time. However, each peak occurs at a different time. We found that hot electron ponderomotive potential peaks early and it matches closely with the time of wave breaking in the simulation system. This is verified by following the evolution of EASWs after the initiation of the process of wave steepening. The ponderomotive frequency of the hot electrons in comparison with the other two species is depicted in Fig. 7(c). The ponderomotive frequencies of all the species are found to be increased at the time of wave breaking as reported by Kakad and Kakad.[25]
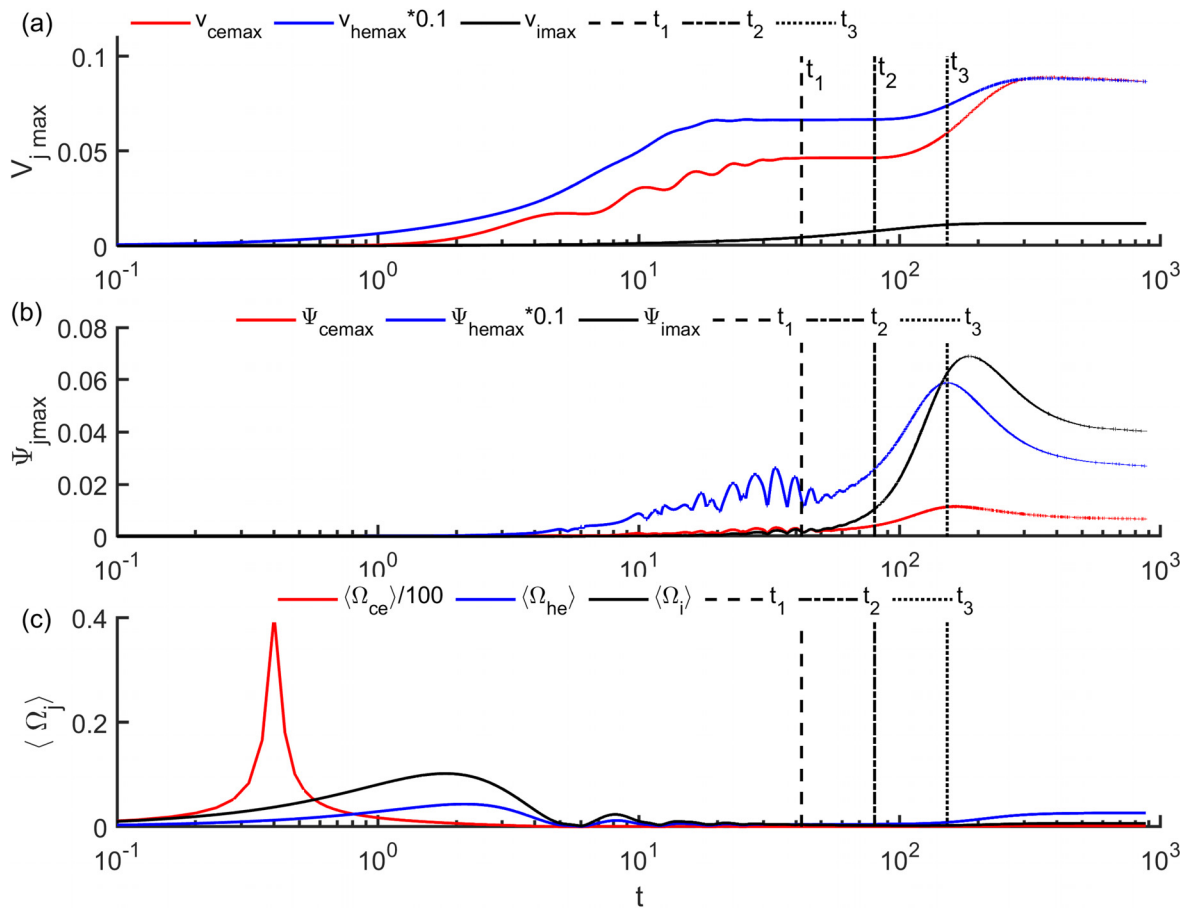
FIG. 7. Variation of (a) maximum velocities (V_{jmax}), (b) maximum ponderomotive potentials (Ψ_{jmax}), and (c) ponderomotive frequencies (Ω_j) of the cold electron, hot electron, and ion with time for run-1. The vertical dashed, dashed-dotted, and dotted lines represent the time of formation of two EA pulses (at $t_1 = 46$), time of initiation of wave steepening (at $t_2 = 80$), and time of wave breaking (at $t_3 = 152$) for run-1, respectively.

In Fig. 7(a), it is noted that all the species accelerate to the higher velocities in the course of formation of two EA wave pulses. The hot electron gains the momentum faster as compared to cold electron and ions. As discussed earlier, we find that the response of the ion is very slow. The maximum ponderomotive potential of all the species shows a gradual increase around the time of the formation of two EA wave pulses, and it increases rapidly during the process of steepening of the wave. A closer view of Fig. 7(b) shows that the ponderomotive potential of the hot electron peaks close to the time of initiation of the wave breaking, while the ponderomotive potential of the cold electrons and ion maximizes at somewhat later time. The amplitude of the ponderomotive potential associated with the hot electron is greater than that of the other two species. This indicates the ponderomotive potential associated with the species that drive the EA wave peaks at the time of the wave breaking. To confirm this tendency, we also examine the maximum ponderomotive force (F_p^{max}) acting on the rightward propagating EA pulse. We have obtained the maximum force acting on the leading and trailing sides of the EASW pulse and plotted separately in Fig. 8. The animation of the spatial variation of the ponderomotive force acting on the hot electron fluid is shown in supplementary material (file A3).

It may be noted that $+F_p^{max}$ ($-F_p^{max}$) is acting on the trailing (leading) side of the EA pulse. Figure 8 shows the maximum ponderomotive force acting on all three species in the rightward ($+x$) direction [Fig. 8(a)] and the leftward ($-x$) direction [Fig. 8(b)] around the position of the EA pulse. The vertical lines in this figure represent times t_1, t_2, and t_3 as discussed earlier for Fig. 7. The maximum ponderomotive force acting on all three species on both the sides of the wave pulse rapidly grow during its steepening. It is observed that the ponderomotive force acting on all three species in the leftward direction is larger in magnitude as compared to that in the rightward direction. In other words, the ponderomotive force on the leading edge (the edge that gets steeper) of the EA pulse is larger as compared to the trailing edge. The ponderomotive force acting on the hot electron along both sides of the pulse maximizes at the time of initiation of the wave breaking. The difference in maximum ponderomotive force (i.e., ΔF_p^{max}) acting on the leading and trailing edges of the hot electron, cold electron, and ion density humps associated with the EA pulse propagating in the $+x$ direction is shown in Fig. 8(c). It may be noted that the maximum imbalance in the ponderomotive force is experienced around times of 149, 157, and 173 for the hot electron, cold electron, and ion, respectively. The ponderomotive force acting on the
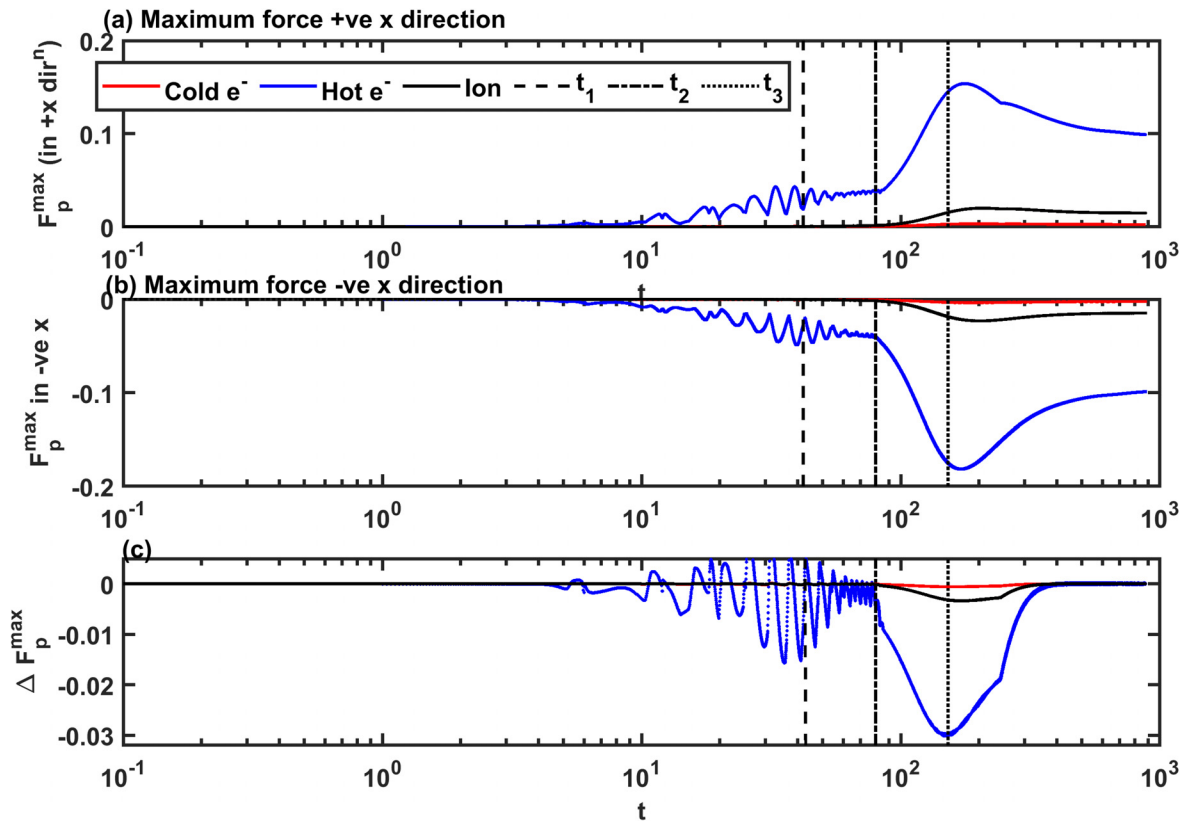
FIG. 8. The maximum ponderomotive force (F_p^{max}) acting on all three species in the rightward ($+x$) direction (panel-a) and the leftward ($-x$) direction (panel-b) around the position of the rightward propagating EA wave pulse in the simulation run-1. (Panel-c) shows the difference between the maximum ponderomotive force (ΔF_p^{max}) acting in the rightward and leftward directions of the EA pulse. The vertical dashed, dashed-dotted, and dotted lines represent the time of formation of two EA pulses ($t_1 = 46$), time of initiation of wave steepening ($t_2 = 80$), and time of wave breaking ($t_3 = 152$) for run-1, respectively.

hot electron at leading and trailing edges of the EA pulse is largely imbalanced at the time of wave breaking, which is clearly evident from Fig. 8(c).

We have examined the maximum kinetic energy associated with all species and the maximum potential energy in the simulation run-1, which is depicted in Fig. 9. The hot electron fluid gains the kinetic energy quiet earlier as compared to the cold electron and ion fluid. It is seen that the kinetic energy of the cold electron and ion gradually increases during the formation of the initial two EA pulses in the simulation system. The ion kinetic energy gains maximum around the time of the initiation of the wave breaking, while the maximum kinetic energy of the cold and hot electrons is found to rapidly grow at the same time interval. The electrostatic energy in the system gradually increases in the course of wave steepening. This energy rapidly enhanced around the time of wave breaking, which is due to the increase in the electrostatic potential at the time of wave breaking.

Similar to run-1, we have identified the steepening and the wave breaking times of the EA wave pulse for run-2 and run-3. Figure 10 depicts the maximum electrostatic potential and the phase speed of the EA waves in the system for simulation runs-1, 2, and 3. In this figure, the vertical dashed-dotted and dashed lines indicate the steepening and breaking time of the EA wave pulse, respectively. The EA
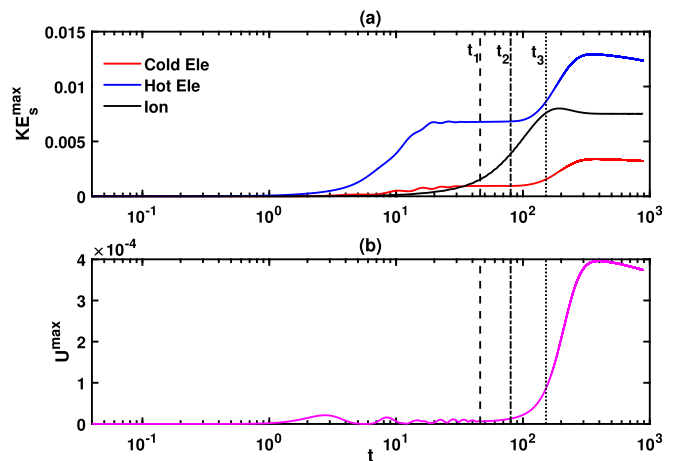
FIG. 9. Evolution of (a) maximum kinetic energy (U_{KE}^{max}) associated with the cold electron, hot electron, and ion fluid. (b) Evolution of maximum electrostatic energy (U^{max}) in the simulation run-1. Vertical dashed, dashed-dotted, and dotted lines represent the time of formation of two EA pulses ($t_1 = 46$), time of initiation of wave steepening ($t_2 = 80$), and time of wave breaking ($t_3 = 152$) for run-1, respectively.
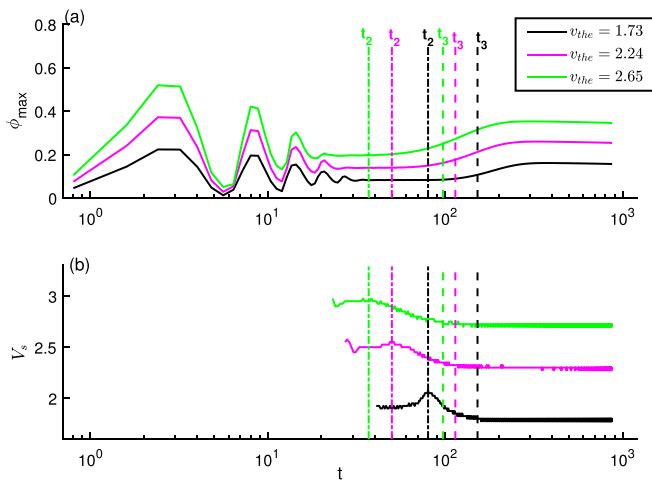
FIG. 10. (a) Evolution of the maximum electrostatic potential (ϕ_{max}) and (b) the phase velocity (V_s) of the EA wave in the simulation run-1, run-2, and run-3. The vertical dashed-dotted and dashed lines represent the time of initiation of wave steepening (t_2) and the time of wave breaking (t_3) for run-1, run-2, and run-3, respectively.

wave steepening (breaking) time noted for run-1, run-2, and run-3 is 80, 50, and 37 (152, 114, and 97), respectively. From this figure, it is observed that the steepening of the EA wave pulse occurs earlier in the plasma with higher hot electron temperature. We have plotted the evolution of ponderomotive potential associated with all species in all

three runs in Fig. 11. This figure confirms again that the ponderomotive potential associated with the hot electrons that drive the EA mode maximizes at the time of wave breaking.

IV. CONCLUSIONS

In the present study, our main goal is to verify whether the earlier proposed proxies (viz., phase speed of the wave and ponderomotive potential associated with plasma species) to identify the steepening and breaking of ion acoustic solitary waves[25] in plasmas are valid for EASWs or not. We have discussed the phenomenon of wave steepening and breaking of the EA waves in a plasma consisting of the cold electrons, hot electrons, and ions. We have successfully demonstrated the steepening and breaking of the electron acoustic wave in three-species plasma and verified these proxies. The simulation of the breaking of EA waves discussed in this paper also pointed out the role of ponderomotive force in the breaking of EA waves in plasma.

The fluid simulation is performed for three different thermal velocities of the hot electrons keeping other plasma parameters fixed. We found that the IDP in the electron and ion equilibrium densities evolves into two unstable electron acoustic pulses which later steepens and breaks into two chains of EASW pulses. In these chains, multiple stable solitary pulses with descending amplitude and phase speed in the spatial domain are formed. The number of pulses in each chain depends on the temperature of the hot electrons. The plasma with higher hot electron temperature supports a fewer number of EA wave pulses in comparison with the plasma with lower hot electron temperature. Our simulation evidences that the onset time of the steepening and breaking of the EA waves is inversely proportional to the
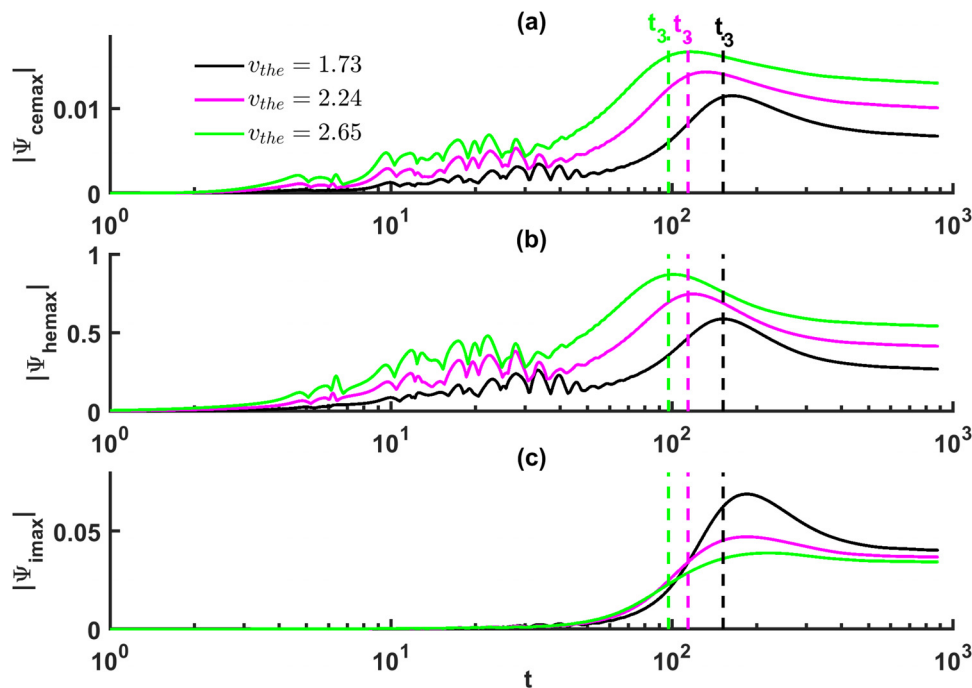
FIG. 11. Evolution of ponderomotive potential associated with the (a) cold electron, (b) hot electron, and (c) ion for simulation runs-1, 2, and 3. In each panel, the vertical dashed lines represent the time of initiation of wave breaking (t_3) for run-1, run-2, and run-3. The time at which the peak appeared in the ponderomotive potential of the hot electron coincides with the time of wave breaking.

temperature of the hot electron. In the present study, we have used only the one set of perturbation parameters (i.e., $\Delta n = 0.5$ and $l_0 = 30$). However, consideration of different perturbation parameters will change the breaking time as well as the characteristics of evolved EASW pulses in the simulation.

We have examined the phase speed, maximum ponderomotive force, ponderomotive frequency, and the ponderomotive potential during the evolution of EASW pulses. All these physical quantities show peculiar behavior at the time of steepening and breaking of the EA wave pulse. It is noticed that the maximum ponderomotive potential of the hot electron maximizes close to the time of wave breaking. This is close to the time when the maximum ponderomotive force experienced at the trailing and leading edges of the hot electron density hump associated with the EA pulse is highly imbalanced. As the magnitude of maximum ponderomotive force at the trailing and leading edges is not the same, the imbalance in the ponderomotive force leads to the wave breaking of the EA pulse. Our simulation shows that the ponderomotive frequency of the electron rapidly starts increasing at the time of the wave breaking. These features are similar to those which were observed in fluid simulation of the breaking of ion acoustic waves in the thermal[25,27] and superthermal[26] plasmas. In conclusion, for the first time, the computer simulation of breaking of the electron acoustic wave has been performed. We believe that the formation of the EASW pulses through breaking of the EA waves could be useful in explaining the spacecraft observations of the series of EASWs in the Earth's magnetosphere.

SUPPLEMENTARY MATERIAL

See the supplementary material for the evolution of a series of EASW pulses in run-1 and run-3 (A1 and A2, respectively) and the animation of the spatial variation of the ponderomotive force acting on the hot electron fluid in run-1 (A3). These animations are created from the data generated from the simulation runs-1 and 3.

ACKNOWLEDGMENTS

REFERENCES

[1] K. Watanabe and T. Taniuti, J. Phys. Soc. Jpn. **43**, 1819 (1977).
[2] S. P. Gary and R. L. Tokar, Phys. Fluids **28**, 2439 (1985).
[3] A. Kakad, B. Kakad, A. Lotekar, and G. Lakhina, Phys. Plasmas **26**, 042112 (2019).
[4] N. Dubouloz, R. Pottelette, M. Malingre, and R. Treumann, Geophys. Res. Lett. **18**, 155, https://doi.org/10.1029/90GL02677 (1991).
[5] R. Pottelette, R. Ergun, R. Treumann, M. Berthomier, C. Carlson, J. McFadden, and I. Roth, Geophys. Res. Lett. **26**, 2629, https://doi.org/10.1029/1999GL900462 (1999).
[6] M. Berthomier, R. Pottelette, L. Muschietti, I. Roth, and C. Carlson, Geophys. Res. Lett. **30**, 2148 (2003).
[7] I. Y. Vasko, O. V. Agapitov, F. S. Mozer, J. W. Bonnell, A. V. Artemyev, V. V. Krasnoselskikh, G. Reeves, and G. Hospodarsky, Geophys. Res. Lett. **44**, 4575, https://doi.org/10.1002/2017GL074026 (2017). 2017GL074026.
[8] J. Hwang, D. Shin, P. Yoon, W. Kurth, B. Larsen, G. Reeves, and D. Lee, Phys. Plasmas **24**, 062904 (2017).
[9] A. Lotekar, A. Kakad, and B. Kakad, J. Geophys. Res.: Space Phys. **124**, 6896, https://doi.org/10.1029/2018JA026303 (2019).
[10] D. Henry and J. Trguier, J. Plasma Phys. **8**, 311 (1972).
[11] M. Hellberg, R. Mace, R. Armstrong, and G. Karlstad, J. Plasma Phys. **64**, 433 (2000).
[12] S. Chowdhury, S. Biswas, N. Chakrabarti, and R. Pal, Phys. Plasmas **24**, 062111 (2017).
[13] G. Lakhina, S. Singh, A. Kakad, M. Goldstein, A. Vinas, and J. Pickett, J. Geophys. Res.: Space Phys. **114**, A09212 (2009).
[14] G. Lakhina, S. Singh, A. Kakad, and J. Pickett, J. Geophys. Res.: Space Phys. **116**, A10218 (2011).
[15] H. Matsumoto, H. Kojima, T. Miyatake, Y. Omura, M. Okada, I. Nagano, and M. Tsutsui, Geophys. Res. Lett. **21**, 2915, https://doi.org/10.1029/94GL01284 (1994).
[16] A. Kakad, S. Singh, R. Reddy, G. Lakhina, and S. Tagare, Adv. Space Res. **43**, 1945 (2009).
[17] C. Dillard, I. Vasko, F. Mozer, O. Agapitov, and J. Bonnell, Phys. Plasmas **25**, 022905 (2018).
[18] M. Berthomier, R. Pottelette, M. Malingre, and Y. Khotyaintsev, Phys. Plasmas **7**, 2987 (2000).
[19] A. Mamun and P. Shukla, J. Geophys. Res.: Space Phys. **107**, 1135, https://doi.org/10.1029/2001JA009131 (2002).
[20] G. Lakhina, A. Kakad, S. Singh, and F. Verheest, Phys. Plasmas **15**, 062903 (2008).
[21] G. S. Lakhina, S. V. Singh, A. P. Kakad, F. Verheest, and R. Bharuthram, Nonlinear Processes Geophys. **15**, 903 (2008).
[22] A. Kakad, S. Singh, R. Reddy, G. Lakhina, S. Tagare, and F. Verheest, Phys. Plasmas **14**, 052305 (2007).
[23] G. S. Lakhina, S. Singh, and A. Kakad, Adv. Space Res. **47**, 1558 (2011).
[24] A. Kakad, Y. Omura, and B. Kakad, Phys. Plasmas **20**, 062103 (2013).
[25] A. Kakad and B. Kakad, Phys. Plasmas **23**, 122101 (2016).
[26] A. Lotekar, A. Kakad, and B. Kakad, Phys. Plasmas **24**, 102127 (2017).
[27] B. Kakad, A. Kakad, and Y. Omura, Phys. Plasmas **24**, 102122 (2017).
[28] S. Maharaj, R. Bharuthram, S. Singh, and G. Lakhina, Phys. Plasmas **19**, 122301 (2012).
[29] B. Kakad, A. Kakad, and Y. Omura, J. Geophys. Res.: Space Phys. **119**, 5589, https://doi.org/10.1002/2014JA019798 (2014).
[30] Y. Omura and J. L. Green, J. Geophys. Res.: Space Phys. **98**, 9189, https://doi.org/10.1029/92JA02901 (1993).
[31] A. Kakad, B. Kakad, C. Anekallu, G. Lakhina, Y. Omura, and A. Fazakerley, J. Geophys. Res.: Space Phys. **121**, 4452, https://doi.org/10.1002/2016JA022365 (2016).
[32] A. Lotekar, A. Kakad, and B. Kakad, Phys. Plasmas **23**, 102108 (2016).
[33] A. Kakad, A. Lotekar, and B. Kakad, Phys. Plasmas **23**, 110702 (2016).